Optimizing Thermoelectric Properties of Type-I and Type-II Nodal Line Semimetals

Ahmad R. T. Nugraha[1,2]

[1]Research Center for Quantum Physics, National Research and Innovation Agency (BRIN), South Tangerang 15314, Indonesia
[2] Department of Engineering Physics, Telkom University, Bandung 40257, Indonesia

E-mail: `ahmad.ridwan.tresna.nugraha@brin.go.id`

Abstract. We investigate the thermoelectric (TE) properties of nodal line semimetals (NLSs) using a combination of semi-analytical calculations within Boltzmann's linear transport theory and the relaxation time approximation, along with first-principles calculations for the so-called type-I and type-II NLSs. We consider the conduction and valence bands that cross near the Fermi level of these materials through first-principles calculations of typical type-I (TiS) and type-II (Mg_3Bi_2) NLSs and use the two-band model fit to find the Fermi velocity v_F and effective mass m that will be employed as the initial energy dispersion parameters. The optimum curvature value for each energy band is searched by tuning both v_F and m to improve the TE properties of the NLSs. By systematically comparing all of our calculation results, we observe that tuning v_F significantly improves TE properties in both types of NLS compared to tuning m. We also find that in all TE metrics, the type-I NLS surprisingly can surpass the type-II NLS, which seems counter-intuitive to the fact that within the two-band model, the type-I NLS contains a parabolic band while the type-II NLS possesses a higher-order, Mexican-hat band. Our study demonstrates that optimizing the curvature of energy bands by tuning v_F can significantly improve the TE performance of NLSs. This approach could guide future efforts in exploring other semimetals as potential TE materials by manipulating their band structures.

Keywords: Thermoelectricity, Nodal line semimetals, Two-band model, Boltzmann transport

1. Introduction

Among the primary energy sources such as gas, oil, and coal that are consumed by humans, it has been estimated that only one-third is used effectively, and two-thirds is wasted, most of which are in the form of heat [1–4]. This form of energy can be converted into useful electrical energy through the so-called thermoelectric (TE) materials. Unfortunately, TE devices often have lower efficiency than most energy conversion schemes. One can assess the TE performance through some parameters such as figures of merit: $ZT = S^2\sigma T/\kappa$, where S is the Seebeck coefficient, σ is the electrical conductivity, T is the operating temperature, and κ is the total thermal conductivity. The thermal conductivity here is a sum of the electronic thermal conductivity (κ_e) and the lattice thermal conductivity (κ_{ph}), $\kappa = \kappa_e + \kappa_{ph}$. The figure of merit is also proportional to the power factor (PF) by the following relation: $ZT = \mathrm{PF} \cdot T/\kappa$, where $\mathrm{PF} = S^2\sigma$. From this expression, we can see that a good TE material should possess good electrical conduction and thermal isolation. In other words, one should maximize the Seebeck coefficient and electrical conductivity to obtain a good TE material, while simultaneously, the thermal conductivity should be minimized. Unfortunately, σ and κ are strongly coupled with each other, hence making it difficult to find the material with high ZT [5–13]. The interplay among these parameters is primarily governed by the Wiedemann-Franz law, which states that the ratio between σ and κ_e is constant. Therefore, obtaining a material with high σ while possessing low thermal conductivity κ is very challenging since κ also increases when σ is enhanced.

Many attempts to decouple the interdependent TE parameters have been proposed to obtain as large ZT as possible for various materials. Some examples of such efforts are carrier concentration optimization [14, 15], nanostructuring materials [16–20], band convergence engineering [21, 22], and hierarchical architecture consideration [23, 24]. Of various methods used to scan potential TE materials, the band engineering methods such as tuning the gap [25] and the effective mass [26–28] in terms of the curvature of the band could be effective because these methods use a relatively cheap computational method by considering only the energy dispersion relation $E(k)$ and the scattering lifetime $\tau(E)$. By doing band-gap tuning or changing the combination of the band structure, one can obtain the optimized structure that will give better TE properties. Several works related to band engineering method have been performed for many types of band structures, such as pudding-mold bands [29–33], parabolic bands [34–36], and the linear Dirac bands [37, 38].

Metals and semimetals are usually not considered as good TE materials due to their poor performance originating from the absence of the energy gap which makes the contributions of electrons and holes in the Seebeck coefficient cancel each other. By contrast, the existence of the heavy bands alongside the Dirac bands gives a high PF value in a semimetal like CoSi [35]. Recently, materials with non-trivial band topology such as the nodal line semimetals (NLSs) [39–43], in which the conduction and valence bands intersect in the form of a line (called the nodal line), have received some attention due to their unique properties and characteristics. The NLSs can be classified into type-I and type-II NLSs based on the slopes of the bands along their nodal lines. The type-I NLS possesses two bands with oppositely aligned slopes near the nodal line and one of its bands is tilted slightly, while the type-II NLS has bands with the same slope near the nodal line because one of its bands is completely tipped over [44]. Other works have also shown that some NLS phases found in Nb_3GeTe_6 [45] or $YbMnSb_2$ [46] might be promising for TE applications with a Seebeck coefficient twice that of normal metals.

It should be noted that the existence of an intersection between a heavy band and Dirac bands at the Fermi level is found to enhance PF due to the improved electron-phonon scattering in the form of a sharp spike density of states (DOS) [34,47]. Specifically, the existing heavy band acts as a filter for the low-energy carriers to be excited [48, 49]. This unbalanced condition will lead to the Seebeck coefficient enhancement [50]. However, the effects of specific electronic band properties such as band curvature and slope on TE properties of NLS type-I are yet unknown. Furthermore, we wonder that although the type-II NLS was claimed to be a promising TE material [51], a systematic comparison of TE properties between type-I and type-II NLSs is not available. Regarding this fact, we are fascinated to find out which type of NLSs will have the higher enhancement of TE performance.

In this work, we will discuss the TE properties of type-I (type-II) NLS materials by using TiS and Mg_3Bi_2 as model materials for each type, respectively. We calculate TE properties by employing a two-band model where we consider two energy bands of each NLS, namely conduction and valence bands, near the Fermi level. Then, we will tune the value of energy dispersion parameters from each band which also alters the shape of the band itself, and see its implication on the TE properties of each NLS. As we will see later, it will greatly affect the TE properties of the NLSs. The rest of the paper is organized as follows. In Section 2, we show the model of the band structure that is considered here for both types of NLSs from the energy dispersion and DOS for both bands to the semi-analytical methods used here to obtain TE properties within the relaxation time approximation (RTA). We also show the computational parameters used here to do the first-principles calculations. Section 3 contains our results from the model; it consists of two subsections that discuss the TE properties of type-II and type-II NLSs, respectively. This paper is concluded in Section 4.

2. Model and Methods

In this section, we begin by outlining the band structure model for each type of NLS considering the energy dispersion of each band. Then, we will show how to apply this model to our semianalytical calculations. Lastly, we will briefly outline the computational parameter used in our first-principles calculations.

2.1. Two-band model

The TE properties can be calculated using the Boltzmann transport theory with RTA. In this approach, we express the TE properties (Seebeck coefficient, electrical conductivity, and electron thermal conductivity) in terms of the TE integrals $\mathcal{L}_i$ as [38, 45, 46, 52, 53]

$$S = \frac{1}{eT}\frac{\mathcal{L}_1}{\mathcal{L}_0} \tag{1}$$

$$\sigma = e^2\mathcal{L}_0, \tag{2}$$

and

$$\kappa_e = \frac{1}{T}\left(\mathcal{L}_2 - \frac{\mathcal{L}_1^2}{\mathcal{L}_0}\right), \tag{3}$$

respectively. Where $\mathcal{L}_i$ depends on the transport properties of the material according to

$$\mathcal{L}_i = \int \tau v^2 g(E) \left(-\frac{\partial f}{\partial E}\right) (E-\mu)^i dE. \tag{4}$$

In Eq. (4), $i = 0, 1, 2$, τ is the relaxation time, $v = \hbar^{-1}|\boldsymbol{\nabla}_{\mathbf{k}} E/\sqrt{3}|$ is the electron longitudinal velocity, $g(E)$ is the density of states (DOS), and $f(E)$ is the Fermi-Dirac distribution:

$$f(E) = \frac{1}{1 + \exp[(E-\mu)/k_B T]} \tag{5}$$

with its partial derivative with respect to energy E:

$$\frac{\partial f}{\partial E} = -\frac{\exp\left[(E-\mu)/k_B T\right]}{(1+\exp[(E-\mu)/k_B T])^2} \left(\frac{1}{k_B T}\right) \tag{6}$$

where k_B, μ, and T is Boltzmann constant, chemical potential, and temperature, respectively. Eq. (4) is often computed by integration of all bands available over the entire range of energy $E = [-\infty, \infty]$. Nevertheless, for a large number of materials, the thermoelectric characteristics depend mainly on the structure of the electronic bands near the Fermi level [54]. We also need to remember that Eq. (4) is only defined in one band formulation.

Since we consider two bands as the main contributors to the TE properties, we break down Eq. (4) as the sum of conduction and valence band contributions, i.e., [52]

$$\mathcal{L}_{c,i} = \int_{E_{0,c}}^{\infty} \tau v^2 g(E) \left(-\frac{\partial f}{\partial E}\right) (E-\mu)^i \, dE, \tag{7}$$

and

$$\mathcal{L}_{v,i} = \int_{-\infty}^{E_{0,v}} \tau v^2 g(E) \left(-\frac{\partial f}{\partial E}\right) (E-\mu)^i \, dE \tag{8}$$

where $E_{0,c}$ and $E_{0,v}$ denote the energy at the band edge of the conduction band and of the valence band, respectively. The procedure is justified as we can see from the previous work [55]. Following this division, the TE properties of our material can also be decomposed into conduction and valence band components, (denoted by c and v subscript respectively), such that the total TE transport coefficients are given by

$$S = \frac{S_c \sigma_c + S_v \sigma_v}{\sigma_c + \sigma_v}, \tag{9}$$

$$\sigma = \sigma_c + \sigma_v, \tag{10}$$

and

$$\kappa_e = \frac{\sigma_c \sigma_v}{\sigma_c + \sigma_v}(S_c - S_v)^2 + (\kappa_{e,c} + \kappa_{e,v}). \tag{11}$$

We will apply Eqs. (7)–(11) to our model of type-I and type-II NLSs.

2.1.1. Type-I NLS

In the type-I NLS, the nodal line is formed when the two bands cross with different slope directions. In this model, we use a Dirac band as the conduction band, and a parabolic band as the valence band. The energy dispersion is given by [56, 57]

$$E_c(k) = \hbar v_F |\mathbf{k}|, \tag{12}$$

for the conduction band and

$$E_v(k) = -\frac{\hbar^2 |\mathbf{k}|^2}{2m} + E_0 \tag{13}$$

for the valence band, respectively, where $\mathbf{k}$ is the electron wavevector, v_F is the Fermi velocity of the Dirac band, m is the effective mass at the edge of the band, and E_0 an energy parameter that is used to determine the position of the valence band maximum. We also define $g(E)$ and $v(E)$ for conduction band as:

$$g_c(E) = \frac{E^2}{\pi^2 \hbar^3 v_F^3}, \tag{14}$$

and

$$v_c(E) = \frac{v_F}{\sqrt{3}} \tag{15}$$

respectively, while for the valence band we define it as

$$g_v(E) = \frac{m}{\hbar^2 \pi^2} \sqrt{\frac{2m(E - E_0)}{\hbar^2}}, \tag{16}$$

and

$$v_v(E) = -\frac{1}{\sqrt{3}} \sqrt{\frac{-2(E - E_0)}{m}}. \tag{17}$$

By substituting the above definitions of $g(E)$ and $v(E)$ into Eqs. (7) and (8), we obtain:

$$\mathcal{L}_{c,i} = \frac{(k_B T)^{i+2}}{3\pi^2 \hbar^3 v_F} \int_0^\infty \tau (x + \eta)^2 \, x^i \, \frac{\exp(x)}{(1 + \exp(x))^2} \, dx, \tag{18}$$

and

$$\begin{aligned} \mathcal{L}_{v,i} =& \frac{2(k_B T)^{i+3/2} \sqrt{2m}}{3\pi^2 \hbar^3} \\ & \times \int_{-\infty}^{\varepsilon_0} \tau (-x - \eta + \varepsilon_0)^{3/2} \, x^i \, \frac{\exp(x)}{(1 + \exp(x))^2} \, dx. \end{aligned} \tag{19}$$

Here, μ and E_0 parameters have been normalized with the thermal energy $k_B T$ such that $\eta = \mu / k_B T$ and $\varepsilon_0 = E_0 / k_B T$, respectively.

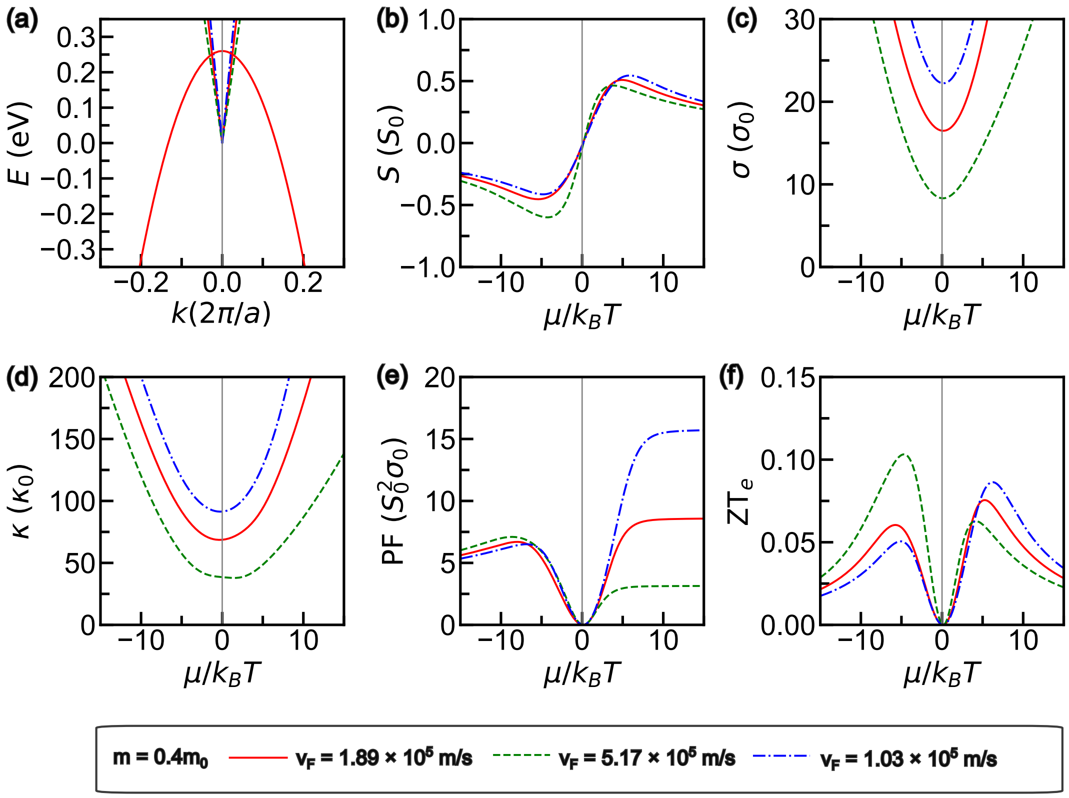

Figure 1. Energy dispersion and TE properties of a type-I NLS model with a varying value of Fermi velocity v_F. For each combination of the two-band model, we show (a) the energy dispersion, (b) Seebeck coefficient S, (c) electrical conductivity σ, (d) electronic thermal conductivity κ_e, (e) power factor (PF), and (f) electronic figure of merit ZT_e. TE properties are plotted versus normalized chemical potential μ/k_BT. The results for S, σ, and κ_e are expressed in the units of S_0, σ_0, and κ_0 respectively.

2.1.2. Type-II NLS

For a type-II NLS, the crossing between the valence and conduction bands occurs when their slopes have the same direction. We model this using the Dirac band for the conduction band and the Mexican-hat-shaped valence band. The energy dispersion of the valence band is given by [58]:

$$E_v(k) = \frac{(\hbar^2 k^2/(4m) - E_1)^2}{E_1} + E_0, \tag{20}$$

where E_1 signifies the depth of the central valley of the central valley of the Mexican-hat band measured from the band edge, m is defined at the valley in the middle of the Mexican-hat band. We define $v(E)$ and $g(E)$ for type-II NLS as:

$$v_\pm(\varepsilon) = \sqrt{\frac{k_BT(\varepsilon_0 - \varepsilon)}{3m}}\sqrt{1 \pm \sqrt{(\varepsilon_0 - \varepsilon)/\varepsilon_1}} \tag{21}$$

and

$$g_{\pm}(\varepsilon) = \frac{4m}{\pi^2\hbar^2}\sqrt{\frac{mk_BT\varepsilon_1}{\hbar^2}}\sqrt{\frac{1 \pm \sqrt{(\varepsilon_0-\varepsilon)/\varepsilon_1}}{(\varepsilon_0-\varepsilon)/\varepsilon_1}}\,. \tag{22}$$

Note that since the Mexican-hat band has a valley in the middle of the band, there are two different values for the velocity, one for the outer ring (with a "+" sign) and the other for the inner ring (with a "−" sign). Substituting Eqs. (21) and (22) into Eq. (8), we obtain the following equations:

$$\begin{aligned}\mathcal{L}_{v,i}^{out} =& \frac{4(k_BT)^{i+3/2}\sqrt{m}}{3\pi^2\hbar^3}\\ &\times \int_{-\infty}^{\varepsilon_0-\eta} \tau\varepsilon_1\sqrt{\varepsilon_0-x-\eta}\left(1+\sqrt{(\varepsilon_0-x-\eta)/\varepsilon_1}\right)^{3/2}\\ &\times x^i\frac{\exp(x)}{(1+\exp(x))^2}\,dx.\end{aligned} \tag{23}$$

for the outer ring and

$$\begin{aligned}\mathcal{L}_{v,i}^{in} =& \frac{4(k_BT)^{i+3/2}\sqrt{m}}{3\pi^2\hbar^3}\\ &\times \int_{\varepsilon_0-\varepsilon 1-\eta}^{\varepsilon_0-\eta} \tau\varepsilon_1\sqrt{\varepsilon_0-x-\eta}\left(1-\sqrt{(\varepsilon_0-x-\eta)/\varepsilon_1}\right)^{3/2}\\ &\times \frac{\exp(x)}{(1+\exp(x))^2}x^i\,dx\end{aligned} \tag{24}$$

for the inner ring. We also normalize μ, E_0, and E_1 parameters with k_BT as $\eta = \mu/k_BT$, $\varepsilon_0 = E_0/k_BT$, and $\varepsilon_1 = E_1/k_BT$, respectively.

We express the units of TE properties as S_0, σ_0, and κ_0. The value of S_0 is the same for type-I and type-II NLSs, i.e., $S_0 = k_B/e \approx 86.17$ μV/K. On the other hand, we distinguish the values of σ_0 and κ_0 depending on the NLS types. For the type-I NLS, we have

$$\sigma_0 = \frac{2\tau e^2(k_BT)}{3\pi^2\hbar^2}\sqrt{\frac{2mk_BT}{\hbar^2}} \tag{25}$$

and

$$\kappa_0 = \frac{2\tau k_B^3T^2}{3\pi^2\hbar^2}\sqrt{\frac{2mk_BT}{\hbar^2}}, \tag{26}$$

while for the type-II NLS we have

$$\sigma_0 = \frac{4\tau e^2(k_BT)}{3\pi^2\hbar^3}\sqrt{\frac{mk_BT}{\hbar^2}} \tag{27}$$

and

$$\kappa_0 = \frac{4\tau k_B^{7/2}T^{5/2}\sqrt{m}}{3\pi^2\hbar^3}. \tag{28}$$

2.2. First-principles simulations

We perform first-principles calculations for both types of NLSs by using Quantum ESPREESSO [59] to obtain the electronic properties that will be used to calculate

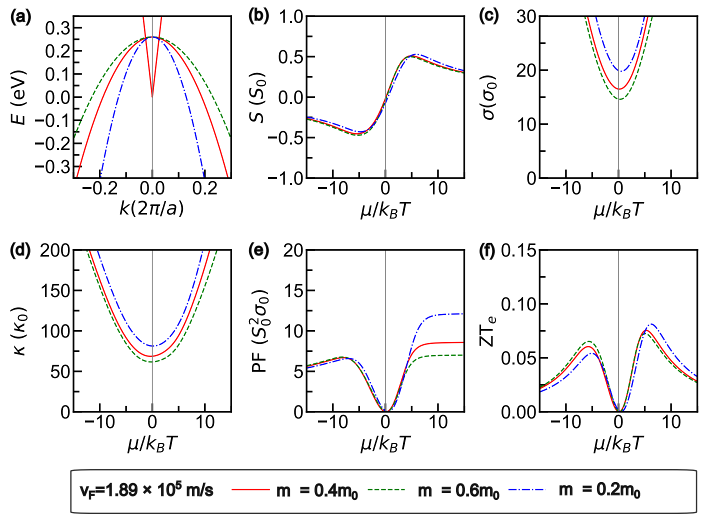

Figure 2. Energy dispersion and TE properties of a type-I NLS model with a varying value of hole effective mass m. For each combination of the two-band model, we show (a) the energy dispersion, (b) Seebeck coefficient S, (c) electrical conductivity σ, (d) electronic thermal conductivity κ_e, (e) power factor (PF), and (f) electronic figure of merit ZT_e. TE properties are plotted versus normalized chemical potential μ/k_BT. The results for S, σ, and κ_e are expressed in the units of S_0, σ_0, and κ_0 respectively.

the TE properties and compare them using the model aforementioned above. In this work, the parameters for the TiS and Mg_3Bi_2 as the model materials for the type-I and type-II NLSs, respectively, are obtained from AFLOWLIB database [60]. For the exchange-correlation functional, we employ the generalized gradient approximation (GGA) [61] of the Perdew-Burke-Ernzerhof (PBE) functional. We set the cutoff energy to 300 eV, which is already sufficient for the convergence. We also calculate the TE properties of the materials using BoltzTraP2 [62], a package that works based on the Boltzmann transport equation to be compared with our model. The electronic properties, i.e., band structures and DOS, from the first-principles calculation can be seen in Appendix A. We fit those band structures with the model energy dispersion for each energy band and tune its curvature through varying v_F and m.

3. Results and discussion

Using Eqs. (12)–(13), (18)–(20), and (23)–(24), we will show the schematic plots of the energy dispersion and discuss the TE properties for both type-I and type-II NLSs. The energy dispersion plots are obtained by fitting the energy level coordinates from the first-principles calculations, from their respective reference materials TiS and Mg_3Bi_2 to our energy dispersion model equations (detailed in Appendix A). This allows us to determine the energy dispersion parameters, v_F and m.

From the fitting, we obtain $v_F = 1.89 \times 10^5$ m/s and $m = 0.4m_0$. These values are used in Eqs. (12)–(13) and (20) to plot the energy dispersion for each energy band, shown in red in panel (a) of Figs. (1)–(4). To investigate the effects of v_F and m on TE properties, we modify the shape of one of the energy bands by selecting higher or lower values of v_F and m than those initially obtained. Specifically, we set

$v_F = 5.17 \times 10^5$ m/s and $v_F = 1.03 \times 10^5$ m/s for the Fermi velocity variation and $m = 0.6m_0$ and $m = 0.2m_0$ for the effective mass variation beyond those initial values obtained from the fitting. Here, m_0 is the free electron rest mass in units of MeV/c^2, i.e., $m_0 = 0.51099895$ MeV/c^2. The altered values of v_F and m are then used in our TE properties calculations, carried out semi-analytically using Eqs. (18)–(19) and (23)–(24) and with the help of SciPy package [63] in Python for solving complicated integrals numerically. In all calculations of the TE properties, the temperature is fixed at $T = 300$ K.

The results for type-I NLS are shown in Figs. 1(a)–(f) and 2(a)–(f), while for type-II NLS are depicted in Figs. 3(a)–(f) and 4(a)–(f). Note that in this work we assess the TE performance of the NLSs in their most optimistic scenario, i.e., when the contribution of κ_{ph} to total κ is neglected. Therefore, the figure of merit ZT is reduced to the electronic figure of merit ZT_e in all of the results discussed in the following sections.

3.1. Type-I NLS

For the type-I NLS, we plot the energy dispersion and TE properties using the parameters mentioned earlier by varying v_F and m values in Figs. 1(a)-(f) and 2(a)–(f), respectively. In the following, we plot the TE properties as a function of a dimensionless normalized chemical potential μ/k_BT to observe the doping effect on TE properties by varying the position of chemical potential. A negative μ/k_BT indicates that this is p-type doping where we move the doping level to the valence band, while a positive μ/k_BT indicates n-type doping which means that the doping level is moved to the conduction band. From Eqs. (25) and (26), we obtain the conductivity units of our type-I NLS model as $\sigma_0 \approx 3.364 \times 10^3$ S/m and $\kappa_0 \approx 7.494 \times 10^{-3}$ W/m.k

In Figs. 1(a) and 2(a), we plot energy dispersion relations of each energy band of our type-I NLS model with varying values of v_F and m, respectively. We observe that in Fig. 1(a) when $v_F = 1.89 \times 10^5$m/s, a tiny increase on the slope of the Dirac band. On the other hand, when $v_F = 1.03 \times 10^5$ the Dirac band becomes slightly steeper as shown in blue color in Fig. 1(a). Even though tuning the value of v_F only makes a slight change in the slope of the Dirac band, it does however greatly affect all TE properties values as we see in panels (b)–(f) of Fig. 1. Next, in Fig. 2 we see that changing m greatly affects the shape of the parabolic band. When $m = 0.2m_0$, the parabolic band becomes a light band, while when $m = 0.6m_0$, the parabolic band becomes a heavy band [55]. Unfortunately, these great changes in the shape of the parabolic band do not affect TE properties compared to v_F tuning. In the following part, we will consider how the changes in the shapes of these energy bands affect each of the TE properties.

First, we consider the Seebeck coefficient S for our type-I NLS model in panel (b) of Figs. 1 and 2 with varying v_F and m values, respectively. Both figures show an opposite trend in $|S|$ peak value changes in response to energy dispersion parameters tuning. We also observe a trend where $|S|$ peak value becomes negative when μ/k_BT is negative. The value is positive when μ/k_BT is shifted to the right where μ/k_BT has positive values. The same trend is also observed in some materials that also have a parabolic band such as $KCaF_3$ [64]. Initially, we set $v_F = 1.89 \times 10^5$m/s and $m = 0.4m_0$ in both figures as their initial values which are obtained from fitting. Then, we approximate $|S|$ peak value from both figures using methods that are explained in Appendix B. Based on our approximation results in Fig. B.1, we obtain $|S|$ peak

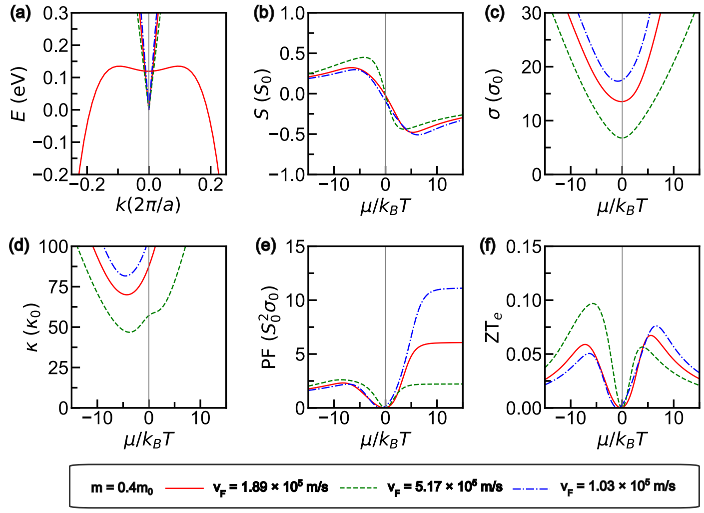

Figure 3. Energy dispersion and TE properties of a type-II NLS model with a varying value of Fermi velocity v_F. For each combination of the two-band model, we show (a) the energy dispersion, (b) Seebeck coefficient S, (c) electrical conductivity σ, (d) electronic thermal conductivity κ_e, (e) power factor (PF), and (f) electronic figure of merit ZT_e. TE properties are plotted versus normalized chemical potential μ/k_BT. The results for S, σ, and κ_e are expressed in the units of S_0, σ_0, and κ_0 respectively.

value of $|0.509S_0|$ for n-type doping and $|0.451S_0|$ for p-type doping. We also observe that there is a significant shift towards $|S|$ when we tune the initial value of v_F. When we set $v_F = 5.17 \times 10^5$m/s, the doping level shifts to the right, and $|S|$ peak value increases by 32.59% for n-type doping in the left to $|0.598S_0|$ for the p-type doping which also marks the highest overall $|S|$ peak value we obtain for both type of NLSs. We also notice that the increase in v_F greatly affects the $|S|$ peak value in p-type doping more than in n-type doping. The only increase we obtain is when v_F is set to $v_F = 1.03 \times 10^5$m/s where we only witness the S peak value increases of 7.07% which lower than 32.59% increase that we obtain before in the p-type doping.

Next, apparently in Fig. 2(b) tuning m value does not have a significant change in S peak value compared to tuning v_F. As we see from our approximation of $|S|$ peak value in Fig. B.2(a), we only obtain the highest increase in $|S|$ peak value when $m = 0.2m_0$ where $|S|$ peak value increases only by 3.54% to $|0.527S_0|$ for n-type doping. Additionally, we also observe that the doping level does not appear to be moving towards as it is only moved slightly to the left towards its initial position.

Furthermore, we consider the effect of tuning the shape of the energy bands on the magnitude of σ and κ in Figs. 1(c)–(d) and 2(c)–(d), respectively. Based on Fig. 1(c), we observe that both σ and κ increase as the Dirac band steepens, i.e. when $v_F = 1.03 \times 10^5$ m/s. Meanwhile, in 2(c), the increase occurs when the band gets narrower where this is obtained when $m = 0.2m_0$. In the same way, this is also true for PF and ZT_e as can be seen Figs. 1(e)–(f) and 2(e)–(f), respectively. In Fig. B.1(b), initially we obtain the PF value of $|8.56S_0^2\sigma_0|$ from initial v_F value in the n-type doping and $|6.586S_0^2\sigma_0|$ in the p-type doping. We witness 83% increase of PF peak value when we set $v_F = 1.03 \times 10^5$ m/s in which PF peak value becomes $|15.67S_0^2\sigma_0|$ in the n-type doping. This value also marks the highest overall PF peak

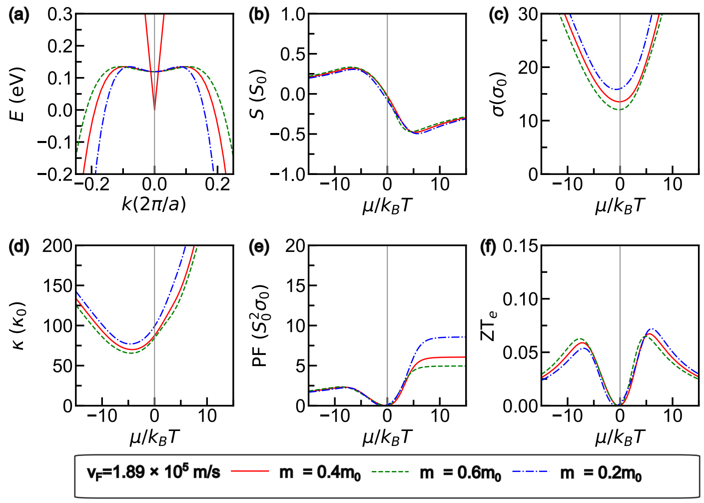

Figure 4. Energy dispersion and TE properties of a type-II NLS model with a varying value of hole effective mass m. For each combination of the two-band model, we show (a) the energy dispersion, (b) Seebeck coefficient S, (c) electrical conductivity σ, (d) electronic thermal conductivity κ_e, (e) power factor (PF), and (f) electronic figure of merit ZT_e. TE properties are plotted versus normalized chemical potential μ/k_BT. The results for S, σ, and κ_e are expressed in the units of S_0, σ_0, and κ_0 respectively.

value from both types of NLSs. Unfortunately, in Fig. B.2(b) the highest PF peak value we obtain 41.18% in the n-type doping where PF peak value is $|12.085 S_0^2\sigma_0|$ also when $v_F = 1.03 \times 10^5$m/s. Regarding the ZT_e, from Fig. B.1(c) we initially obtain the ZT_e value of 0.075 for the n-type doping and 0.060 for the p-type doping when $v_F = 1.89 \times 10^5$ m/s. Then, we obtain 71.67% increase of ZT_e to 0.103 when $v_F = 1.03 \times 10^5$m/s in the p-type doping. This increase is the highest overall from both types of NLSs and also the highest ZT_e value compared to type-II NLS. On the other hand, when we tune the m we only obtain 8.33% increase of ZT_e value to 0.065 as can be seen in Fig. B.2(c).

We suspect that those increases aforementioned above results from the term $\frac{(k_BT)^{i+2}}{3\pi^2\hbar^3 v_F}$ in Eq. (18) and the term $\frac{2(k_BT)^{i+3/2}\sqrt{2m}}{3\pi^2\hbar^3}$ in Eq. (19) for the Dirac band and parabolic band, respectively. This increase also agrees with the Wiedemann-Franz law.

3.2. Type-II NLS

We plot the energy dispersion and TE properties for type-II NLS for by varying the value of v_F and m in Figs. 3(a)–(f) and 4(a)–(f), respectively. For TE properties calculation we obtain from Eqs. (27) and (28) $\sigma_0 \approx 4.757 \times 10^3$ S/m and $\kappa_0 \approx 5.299 \times 10^{-3}$ W/m.k.

From Figs. 3(a) and 4(a), we observe that the given values of v_F and m greatly affect the slope of the Dirac band and the depth of the Mexican-hat band NLS type-II. For the Dirac band, it can be seen in Fig. 3(a) that the slope of the Dirac band will increase when $v_F = 5.17 \times 10^5$m/s. On the other hand, when $v_F = 1.03 \times 10^5$m/s, the Dirac band will get steeper and narrower. For the Mexican-hat band in Fig. 4(a), the effect of the value of m on the depth of the Mexican-hat band is as follows. As $m = 0.6m_0$, the depth of this band will increase. Contrarily, if $m = 0.2m_0$, the Mexican hat band will lose its depth. In the following part, we consider the effects of these energy band adjustments on type-II NLS TE properties.

First, we consider S in Figs. 3(b) and 4(b). Initially, in Fig. B.3(a) by the initial dispersion energy parameters, we obtain $|S|$ peak value of $|0.478S_0|$ for n-type doping and $|0.319S_0|$ for p-type doping, respectively. We obtain the highest $|S|$ peak value increase of about 40.75% to $|0.449S_0|$ when $v_F = 5.17 \times 10^5$ m/s for the p-type doping. This positive value may be attributed to the inclination of the Dirac band. Accordingly, it is better to increase v_F since it will also increase carrier mobility because the S is also related to carrier mobility. In contrast, it also seems that tuning m doesn't improve $|S|$ peak value significantly compared to tuning v_F as seen in Fig. B.4(a). The highest increase we obtain only 3.56% to $|0.495S_0|$ when $m = 0.2m_0$ for the n-type doping. Therefore, we believe that tuning the shape of the Mexican hat band through m tuning is not a good idea to improve the TE properties of our type-II NLS model compared to tuning the slope of the Dirac band.

Next, in Figs. 3(c)–(d) and 4(c)–(d) we can see that tuning v_F and m also cause changes in σ and κ. Even though the increase is not as drastic as in the type-I NLS model, it still greatly affects PF and $\mathrm{ZT_e}$ as we explain in the later part. This increase is probably caused by the term $\frac{(k_BT)^{i+2}}{3\pi^2\hbar^3 v_F}$, $\frac{4\tau(k_BT)^{i+3/2}\sqrt{m}}{3\pi^2\hbar^3}$, and $\frac{4\tau(k_BT)^{i+3/2}\sqrt{m}}{3\pi^2\hbar^3}$ in Eqs. (18), (24), and (23), respectively.

Furthermore, in Figs. 3(e) and 4(e) where we consider the PF we obtain the respective PF of $|6.055S_0^2\sigma_0|$ for n-type doping and $|2.312S_0^2\sigma_0|$ for p-type doping using the initial energy dispersion parameters as can be seen in Figs. B.3(b) and 4(b). The increase of PF peak value that occurs in Fig. B.3(e) is about 83% larger than the initial value when $v_F = 1.03 \times 10^5$m/s which changes PF peak value to $|11.085S_0^2\sigma_0|$ for n-type doping. We also observe changes in PF peak value caused by m tuning, although not as large as when we tune the v_F. We obtain a PF peak value increase of 41.29% to $|8.555S_0^2\sigma_0|$ when $m = 0.2m_0$, while for the p-type doping the increase we obtain is not significant. We observe that those increases in PF might be caused by a simultaneous increase in σ in panel (c) of Figs. 3 and 4 through the relation $\mathrm{PF} = S^2\sigma$. Therefore, we suggest that tuning v_F is the best option to obtain the optimum value for PF.

Finally, in Figs. 3(f) and 4(f). We obtain the respective ZT_e peak values of 0.067 for n-type doping and $0,059$ p-type doping by using initial energy dispersion parameters From Fig. 3(f), respectively. In Fig. 3(f), We obtain the highest increase in peak value of ZT_e for the p-type doping when $v_F = 5.17 \times 10^5$ m/s. We obtain 64.41% increases in peak ZT_e value to 0.097. Meanwhile, we only obtain the highest ZT_e increase of 7.46% when $m = 0.2m_0$ based on our approximation done in Fig. B.4.

4. Conclusions

We have systematically studied TE properties of NLS type-I and type-II through consideration of energy dispersion shapes by tuning each of the NLS band curvatures. We found that changing the shape of the energy dispersion through slight modifications of its parameters, v_F and m, can drastically affect the TE properties of both types of NLSs. For the Seebeck coefficient S, we obtained the largest S peak value in the p-doped type-I NLS of about $|0.598S_0|$, where $S_0 \approx 86.17$ μV/K. On the other hand,

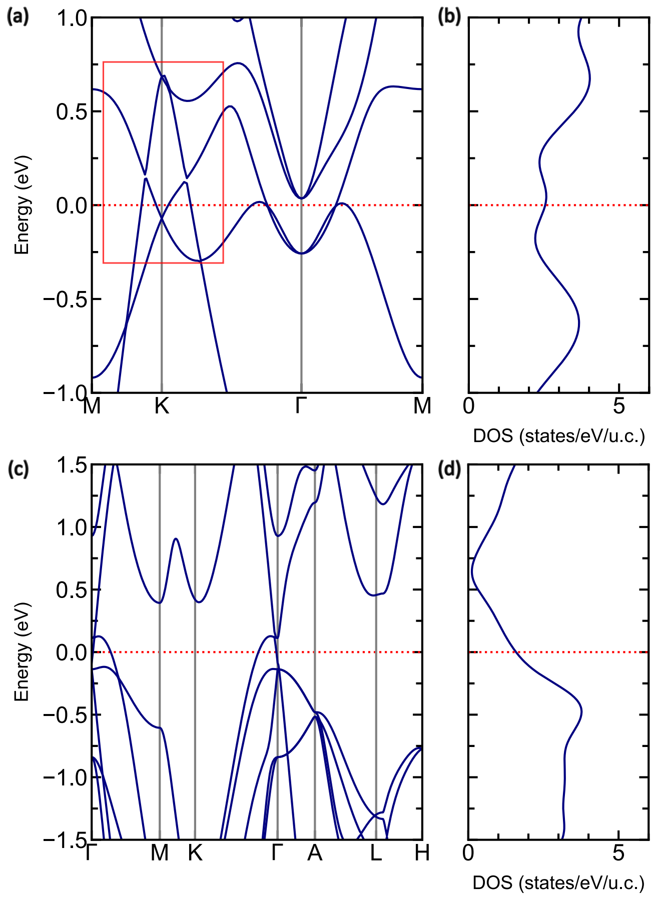

Figure A.1. Electronic properties of NLS reference materials considered in this study: (a-b) TiS and (c-d) Mg_3Bi_2. Panels (a) and (c) show the results for the band structures, while panels (b) and (d) show the results for DOS.

although the largest $|S|$ in the type-II NLS is less than that in the type-I NLS, the largest increase in $|S|$ up to 40.75% is obtained by varying v_F in the p-doped type-II NLS. As for the power factor (PF), we observed about 83% increase in the PFs of both types of NLSs in the n-doped regime, with the type-I NLS achieving the highest overall PF peak value compared to the type-II NLS. Lastly, we recorded a 71.67% increase in ZT_e for the type-I NLS and a 64.41% increase for the type-II NLS under p-type doping. Our work is expected to trigger further calculations to scan other potential TE materials, particularly in the class of semimetals, by manipulating their band structure through the variation of the curvatures of their energy bands.

Acknowledgments

We acknowledge Mahameru BRIN for its HPC facility.

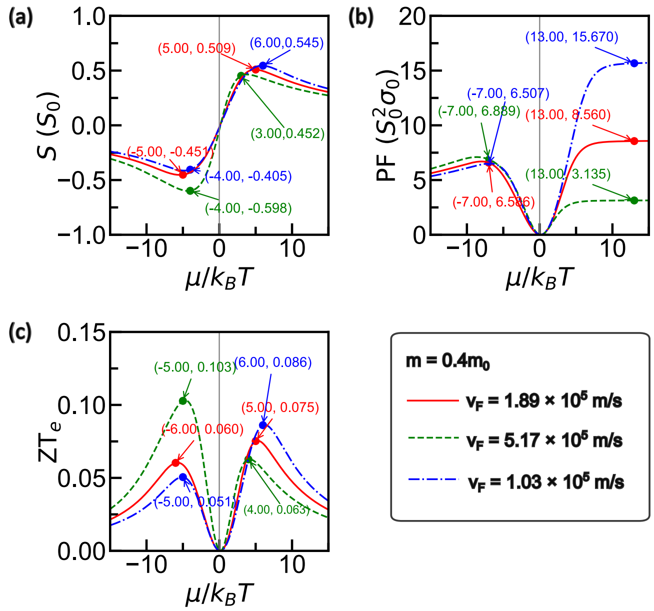

Figure B.1. Approximations of peak values of TE properties for type-I NLS model with varying Fermi velocity v_F. We show the approximate peak values for (a) Seebeck coefficient S, (b) power factor (PF), and (c) electronic figure of merit ZT_e.

Appendix A. Electronic properties of TiS and Mg_3Bi_2 from first-principles simulations

As mentioned before, we use TiS and Mg_3Bi_2 as our reference materials for type-I and type-II NLS, respectively. In Figs. A.1(a)–(b), we show the electronic properties of TiS. From Fig. A.1(a), we see a band crossing in $\mathrm{M}-\mathrm{K}-\Gamma$ path that confirms that the material belongs to type-I NLS. This also confirms the observation in Ref. [65]. Then, we took the energy band's energy level coordinates to fit it with our model energy dispersion equation and tune its curvature. Next, for Mg_3Bi_2, we show the electronic properties in Figs. A.1(c)–(d). From Fig. A.1, we can see that there is a crossing in $\mathrm{K}-\Gamma-\mathrm{M}$ which confirms that the material is a type-II NLS, consistent with Ref. [44]. Then, we perform a two-band model fitting similar to the case of type-I NLS to obtain the energy dispersion parameters, as mentioned at the beginning of Sec 3.

Appendix B. Peak value approximations for the TE properties

We examine our TE properties calculation results here by approximating its peak value to observe the change in the peak values of the TE properties due to variations of the energy dispersion parameters (m and v_F). The peak values are approximated by numerically interpolating the TE properties using the NumPy package.

In Figs. B.1(a)–(c), we approximate peak values of the TE properties of the type-I NLS model by tuning the Dirac band with varying v_F values. For S in Fig. B.1(a), we find that the initial $|S|$ peak values at $v_F = 1.89 \times 10^5$ m/s are $|0.509S_0|$ for the n-type doping and $|0.451S_0|$ the for p-type doping. As v_F increases

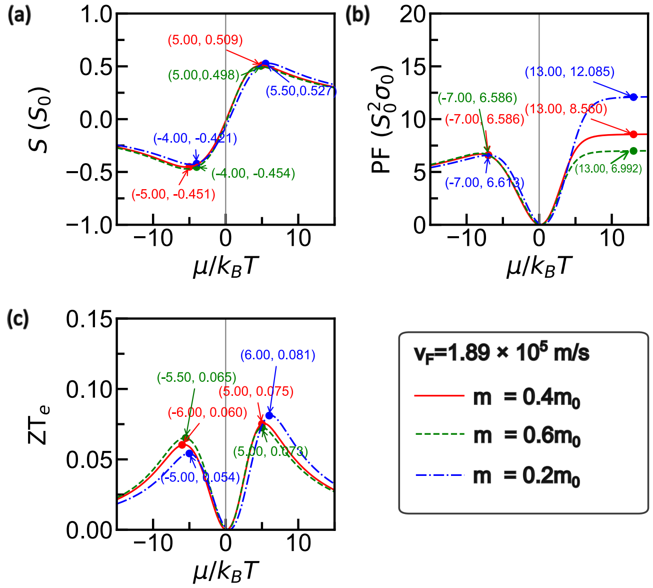

Figure B.2. Approximations of peak values of TE properties for type-I NLS model with varying hole effective mass m values. We show the approximate peak values for (a) Seebeck coefficient S, (b) power factor (PF), and (c) electronic figure of merit ZT_e.

to $v_F = 5.17 \times 10^5$ m/s, the S peak value in the n-type doping decrease by 11.20% to $|0.452S_0|$, while for the p-type doping increases by 32.59% to $|0.598S_0|$. Conversely, reducing v_F to $v_F = 1.03 \times 10^5$ m/s leads to a 7.07% increase in the $|S|$ peak value for the n-type doping ($|0.545S_0|$) and a 10.20% decrease for the p-type doping ($|-0.405S_0|$). These results indicate that modifying the Dirac band shape by tuning v_F can significantly enhance the $|S|$ peak value in p-type doping when v_F is increased while reducing v_F results in a notable decrease.

In Fig. B.1(b), we observe a different trend for the PF peak values. At $v_F = 5.17 \times 10^5$ m/s, the PF peak value for the n-type doping decreases sharply by 63.38% to $|3.135S_0^2\sigma_0|$, while for the p-type doping, it increases slightly by 4.6% to $|6.689^2_0\sigma_0|$. On the other hand, when v_F is reduced to $v_F = 1.03 \times 10^5$ m/s, the PF peak value for the n-type doping increases dramatically by 83% to $|15.67S_0^2\sigma_0|$, whereas for the p-type doping, it decreases modestly by 1.2% to $|6.507S_0^2\sigma_0|$. Therefore, tuning v_F significantly impacts the PF peak value in the n-type doping than in the p-type doping.

Finally, for ZT_e in Fig. B.1(c), we observe the highest overall fluctuations in peak values, with both significant increases and decreases, in the type-I NLS model. The highest increase in ZT_e occurs at $v_F = 5.17\times10^5$m/s where it rises by 71.67%, reaching a peak value of 0.103 which is also the highest ZT_e peak value overall for type-I NLS. Then, the most notable decrease in ZT_e is observed at $v_F = 1.03 \times 10^5$ m/s where it drops by 15% down to 0.051.

Next, we analyze the TE properties peak value of the type-I NLS model by tuning the parabolic band with varying m values in Figs. B.2(a)–(c). From Fig. B.2(a), the $|S|$ peak value decreases slightly by 2.16% at $m = 0.6m_0$ for the n-type doping, while for the p-type doping, it increases marginally by 0.67%, reaching $|0.454S_0|$. At

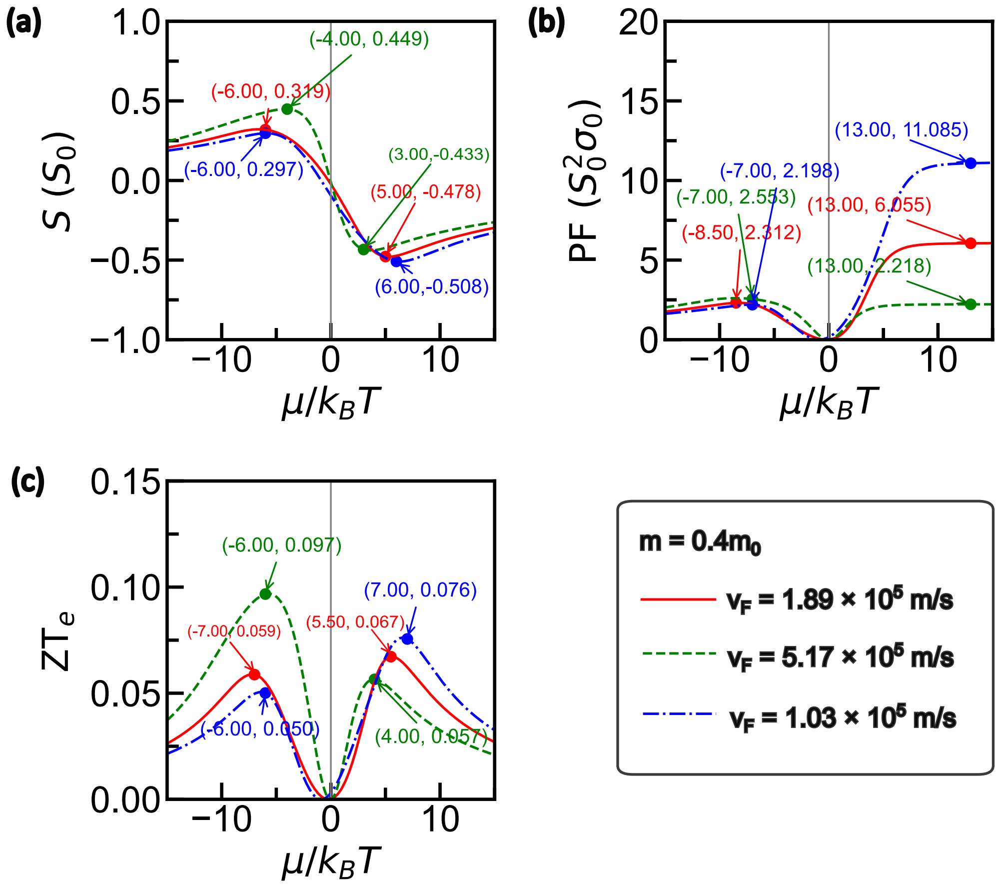

Figure B.3. Approximations of peak values of TE properties for type-II NLS model with varying value of Fermi velocity v_F. We show the approximate peak values for (a) Seebeck coefficient S, (b) power factor (PF), and (c) electronic figure of merit ZT_e.

$m = 0.2m_0$, the $|S|$ peak values show more noticeable changes, with an increase of 3.54% for the n-type doping to $|0.527S_0|$, and a decrease of 6.65% for the p-type doping to $|0.421S_0|$. These results suggest that tuning m has a relatively minor effect on the type-I NLS TE properties, with only small changes observed in the peak values.

In Fig. B.2(b), we see an interesting trend for the PF peak value. At $m = 0.6m_0$, the PF peak value for the n-type doping decreases by 18.32% to $|6.992S_0^2\sigma_0|$, while for the p-type doping, it increases about 0.41% to $|6.613_0^2\sigma_0|$. However, when $m = 0.2m_0$, the PF peak value for the n-type doping increases 41.18% to $|12.085S_0^2\sigma_0|$, whereas for the p-type doping remains at $|6.586S_0^2\sigma_0|$. These results highlight that tuning m primarily only improves the PF in n-type doping. Finally, for ZT_e in Fig. B.2(c), the highest increase can be obtained by tuning m is 8.33% at $m = 0.6m_0$, where ZT_e increases to 0.065 for the p-type doping. The highest ZT_e peak value is obtained at $m = 0.2m_0$, where it increases by 8% to 0.081 in the n-type doping.

In Figs. B.3(a)–(c), we approximate the peak values of TE properties of the type-II NLS model by tuning the v_F. As we see in Fig. B.3(a), when $v_F = 5.17 \times 10^5$ m/s, the

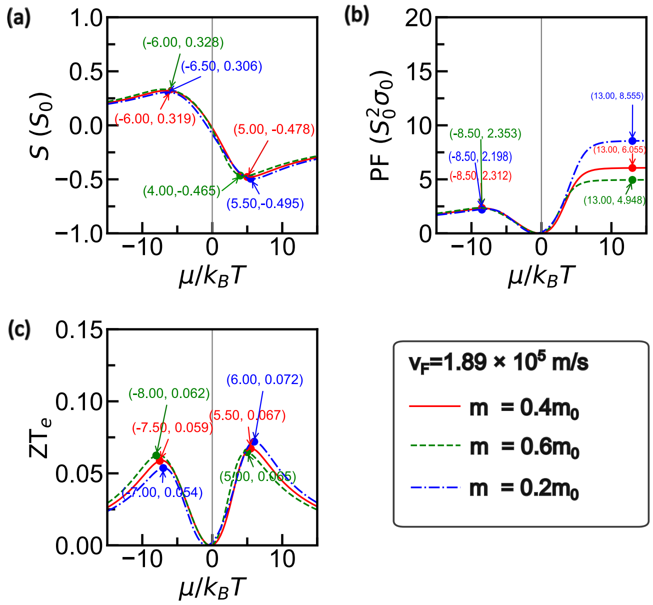

Figure B.4. Approximations of peak values of TE properties for type-II NLS model with varying hole effective mass m values. We show the approximate peak values for (a) Seebeck coefficient S, (b) power factor (PF), and (c) electronic figure of merit ZT_e.

S peak value in the n-type doping decreases by 9.41% to $|0.433S_0|$, while for the p-type doping it increases by 40.75% to $|0.449S_0|$. Contrarily, as $v_F = 1.03 \times 10^5$ m/s, the $|S|$ peak value increases by 6.28% for the n-type doping ($|0.508S_0|$). This $|S|$ increase is the largest and also the highest S peak value overall for the type-II NLS.

Furthermore, from Fig. B.3(b) we observe the PF peak value trend for type-II NLS when v_F is tuned and also obtain that at $v_F = 1.03\times10^5$ m/s the largest PF peak value for type-II NLS is $|11.085S_0^2\sigma_0|$ in the n-type doping which means it increases about 83% relative to the value obtained using the initial energy dispersion parameter. In the type-II NLS, we also notice the same trend as that in the type-I NLS for the PF peak value that tends to be larger in the n-type doping rather than in the p-type doping. The PF peak values in the p-type doping also do not change much when we tune the energy dispersion parameters. Then, based on Fig. B.3(c), we observe the highest overall changes in ZT_e for the type-II NLS at $v_F = 5.17 \times 10^5$m/s, where it rises by 64.41% to 0.097 for the n-type doping. We also see that the changes in ZT_e are more significant in the p-type doping than the n-type doping.

In the following, we examine the peak values of the TE properties for the type-II NLS model by tuning the Mexican-hat band with varying m values in Figs. B.4(a)–(c). Based on Fig. B.4(a), we obtain the highest increase in the $|S|$ peak value by tuning m for type-II NLS of about 3.56% when $m = 0.2m_0$ which changes the $|S|$ peak value to $|0.495S_0|$ for the n-type doping. In Fig. B.4(b), for the PF peak value we obtain the highest increase of 41.29% by tuning m, which makes the PF peak value becomes $8.555S_0^2\sigma_0$ in the n-type doping when $m = 0.2m_0$. On the other hand, for the p-type doping, the change is only 1.77% when $m = 0.2m_0$, an this variation only leads to the PF peak value of about $2.353S_0\sigma_0^2$. Finally, in Fig. B.4(c), the highest increase of

ZT_e we obtain for type-II NLS by tuning m is only 7.46% at $m = 0.2m_0$ where ZT_e increases to 0.072 for the n-type doping.

References

[1] Fitriani, Ovik R, Long B, Barma M, Riaz M, Sabri M, Said S and Saidur R 2016 *Renew. Sustain. Energy Rev.* **64** 635–659

[2] Koumoto K and Mori T 2013 *Thermoelectric nanomaterials* (Berlin, Heidelberg: Springer)

[3] Elsheikh M H, Shnawah D A, Sabri M F M, Said S B M, Hassan M H, Bashir M B A and Mohamad M 2014 *Renew. Sustain. Energy Rev.* **30** 337–355

[4] Zheng X, Liu C, Yan Y and Wang Q 2014 *Renew. Sustain. Energy Rev.* **32** 486–503

[5] Zeier W G, Zevalkink A, Gibbs Z M, Hautier G, Kanatzidis M G and Snyder G J 2016 *Angew. Chem.* **55** 6826–6841

[6] Yang J, Xi L, Qiu W, Wu L, Shi X, Chen L, Yang J, Zhang W, Uher C and Singh D J 2016 *npj Comput. Mater.* **2** 1–17

[7] Jain A, Shin Y and Persson K A 2016 *Nat. Rev. Mater.* **1** 1–13

[8] Zhu T, Liu Y, Fu C, Heremans J P, Snyder J G and Zhao X 2017 *Adv. Mater.* **29** 1605884

[9] He J and Tritt T M 2017 *Science* **357** eaak9997

[10] Gorai P, Stevanović V and Toberer E S 2017 *Nat. Rev, Mater.* **2** 1–16

[11] Mao J, Liu Z, Zhou J, Zhu H, Zhang Q, Chen G and Ren Z 2018 *Adv. Phys* **67** 69–147

[12] Darmawan A, Suprayoga E, AlShaikhi A A and Nugraha A R 2022 *Mater. Today Commun* **33** 104596

[13] Hu J, Tang Z, Liu J, Liu X, Zhu Y, Graf D, Myhro K, Tran S, Lau C N, Wei J *et al.* 2016 *Phys. Rev. Lett.* **117** 016602

[14] Chen Z G, Han G, Yang L, Cheng L and Zou J 2012 *Prog. Nat. Sci.: Mater. Int.* **22** 535–549

[15] Zhou M, Gibbs Z M, Wang H, Han Y, Li L and Snyder G J 2016 *Appl. Phys. Lett.* **109** 042102

[16] Poudel B, Hao Q, Ma Y, Lan Y, Minnich A, Yu B, Yan X, Wang D, Muto A, Vashaee D *et al.* 2008 *science* **320** 634–638

[17] Ma Y, Hao Q, Poudel B, Lan Y, Yu B, Wang D, Chen G and Ren Z 2008 *Nano Lett.* **8** 2580–2584

[18] Xie W, Tang X, Yan Y, Zhang Q and Tritt T M 2009 *Appl. Phys. Lett.* **94**

[19] Xie W, He J, Kang H J, Tang X, Zhu S, Laver M, Wang S, Copley J R, Brown C M, Zhang Q *et al.* 2010 *Nano Lett.* **10** 3283–3289

[20] Yan X, Liu W, Chen S, Wang H, Zhang Q, Chen G and Ren Z 2013 *Adv. Energy Mater.* **3** 1195–1200

[21] Mahan G and Sofo J 1996 *Proc. Natl. Acad. Sci. U.S.A.* **93** 7436–7439

[22] Mao J, Wang Y, Kim H S, Liu Z, Saparamadu U, Tian F, Dahal K, Sun J, Chen S, Liu W *et al.* 2015 *Nano Energy* **17** 279–289

[23] Biswas K, He J, Blum I D, Wu C I, Hogan T P, Seidman D N, Dravid V P and Kanatzidis M G 2012 *Nature* **489** 414–418

[24] Ren G K, Wang S Y, Zhu Y C, Ventura K J, Tan X, Xu W, Lin Y H, Yang J and Nan C W 2017 *Energy Environ. Sci.* **10** 1590–1599

[25] Pei Y, Heinz N A and Snyder G J 2011 *J. Mater. Chem.* **21** 18256–18260

[26] Bilc D, Mahanti S, Quarez E, Hsu K F, Pcionek R and Kanatzidis M 2004 *Phys. Rev. Lett.* **93** 146403

[27] Heremans J P, Wiendlocha B and Chamoire A M 2012 *Energy Environ. Sci.* **5** 5510–5530 ISSN 1754-5692

[28] Pei Y, LaLonde A D, Wang H and Snyder G J 2012 *Energy Environ. Sci.* **5** 7963–7969

[29] Usui H and Kuroki K 2017 *J. Appl. Phys* **121**

[30] Usui H, Suzuki K, Kuroki K, Nakano S, Kudo K and Nohara M 2013 *Phys. Rev. B* **88** 075140

[31] Kuroki K and Arita R 2007 *J. Phys. Soc. Jpn.* **76** 083707–083707

[32] Isaacs E B and Wolverton C 2019 *Phys. Rev. Mater* **3** 015403

[33] Wei S, Wang C, Fan S and Gao G 2020 *J. Appl. Phys* **127**

[34] Xia Y, Park J, Ozoliņš V and Wolverton C 2019 *Phys. Rev. B* **100** 201401

[35] Xia Y, Park J, Zhou F and Ozoliņš V 2019 *Phys. Rev. Appl.* **11** 024017

[36] Adhidewata J M, Nugraha A R, Hasdeo E H, Estellé P and Gunara B E 2022 *Mater. Today Commun.* **31** 103737

[37] Adhidewata J M, Nugraha A R, Hasdeo E H and Gunara B E 2022 *Indones. J. Appl. Phys.* **33** 51–57

[38] Hasdeo E H, Krisna L P A, Hanna M Y, Gunara B E, Hung N T and Nugraha A R T 2019 *J. Appl. Phys* **126** 035109 ISSN 0021-8979

[39] Shao Y, Rudenko A N, Hu J, Sun Z, Zhu Y, Moon S, Millis A J, Yuan S, Lichtenstein A I, Smirnov D, Mao Z Q, Katsnelson M I and Basov D N 2020 *Nat. Phys.* **16** 636–641 ISSN 1745-2481

[40] Rudenko A, Stepanov E, Lichtenstein A and Katsnelson M 2018 *Phys. Rev. Lett.* **120** 216401

[41] Singha R, Pariari A K, Satpati B and Mandal P 2017 *Proc. Natl. Acad. Sci. U.S.A.* **114** 2468–2473
[42] Ali M N, Schoop L M, Garg C, Lippmann J M, Lara E, Lotsch B and Parkin S S 2016 *Sci. Adv.* **2** e1601742
[43] Guan S, Yu Z M, Liu Y, Liu G B, Dong L, Lu Y, Yao Y and Yang S A 2017 *npj Quantum Mater.* **2** 23 ISSN 2397-4648 URL `https://doi.org/10.1038/s41535-017-0026-7`
[44] Zhang X, Jin L, Dai X and Liu G 2017 *J. Phys. Chem. Lett.* **8** 4814–4819
[45] Wang X, Ding G, Khandy S A, Cheng Z, Zhang G, Wang X L and Chen H 2020 *Nanoscale* **12** 16910–16916
[46] Pan Y, Fan F R, Hong X, He B, Le C, Schnelle W, He Y, Imasato K, Borrmann H, Hess C *et al.* 2021 *Adv. Energy Mater.* **33** 2003168
[47] Rudderham C and Maassen J 2021 *Phys. Rev. B* **103** 165406
[48] Bahk J H and Shakouri A 2016 *Phys. Rev. B* **93** 165209
[49] Androulakis J, Todorov I, Chung D Y, Ballikaya S, Wang G, Uher C and Kanatzidis M 2010 *Phys. Rev. B* **82** 115209
[50] Gayner C, Sharma R, Das M K and Kar K K 2016 *J. Appl. Phys* **120**
[51] Hung N T, Adhidewata J M, Nugraha A R and Saito R 2022 *Phys. Rev. B* **105** 115142
[52] Goldsmid H J *et al.* 2010 *Introduction to thermoelectricity* vol 121 (Springer)
[53] Ashcroft N W 1976 *Saunders College, Philadelphia* **120**
[54] Markov M, Hu X, Liu H C, Liu N, Poon S J, Esfarjani K and Zebarjadi M 2018 *Sci. Rep.* **8** 9876
[55] Chasapis T C, Lee Y, Hatzikraniotis E, Paraskevopoulos K M, Chi H, Uher C and Kanatzidis M G 2015 *Phys. Rev. B* **91** 085207
[56] Neto A C, Guinea F, Peres N M, Novoselov K S and Geim A K 2009 *Rev. Mod. Phys.* **81** 109
[57] Ariel V 2012 *arXiv preprint arXiv:1207.4282*
[58] Wickramaratne D, Zahid F and Lake R K 2015 *J. Appl. Phys* **118**
[59] Giannozzi P, Baroni S, Bonini N, Calandra M, Car R, Cavazzoni C, Ceresoli D, Chiarotti G L, Cococcioni M, Dabo I *et al.* 2009 *J. Phys. Condens. Matter* **21** 395502
[60] Curtarolo S, Setyawan W, Wang S, Xue J, Yang K, Taylor R H, Nelson L J, Hart G L, Sanvito S, Buongiorno-Nardelli M *et al.* 2012 *Comput. Mater. Sci.* **58** 227–235
[61] Perdew J P, Chevary J A, Vosko S H, Jackson K A, Pederson M R, Singh D J and Fiolhais C 1992 *Phys. Rev. B* **46** 6671
[62] Madsen G K, Carrete J and Verstraete M J 2018 *Comput. Phys. Commun.* **231** 140–145
[63] Virtanen P, Gommers R, Oliphant T E, Haberland M, Reddy T, Cournapeau D, Burovski E, Peterson P, Weckesser W, Bright J *et al.* 2020 *Nat. Methods* **17** 261–272
[64] Ali A, Rahman A U and Rahman G 2019 *Phys. B: Condens. Matter* **565** 18–24
[65] Xu L, Zhang X, Meng W, He T, Liu Y, Dai X, Zhang Y and Liu G 2020 *Journal of Materials Chemistry C* **8** 14109–14116